A&A 636, A73 (2020)
https://doi.org/10.1051/0004-6361/201936817

Astronomy & Astrophysics

Universal bolometric corrections for active galactic nuclei over seven luminosity decades

F. Duras[1,2,3], A. Bongiorno[2], F. Ricci[4], E. Piconcelli[2], F. Shankar[5], E. Lusso[6,7], S. Bianchi[1], F. Fiore[8,9], R. Maiolino[10], A. Marconi[6], F. Onori[11], E. Sani[12], R. Schneider[13,2], C. Vignali[14,15], and F. La Franca[1]

[1] Dipartimento di Matematica e Fisica, Università Roma Tre, Via della Vasca Navale 84, 00146 Roma, Italy
e-mail: federicaduras@gmail.com
[2] Osservatorio Astronomico di Roma – INAF, Via Frascati 33, 00040 Monteporzio Catone, Italy
[3] Aix Marseille Univ, CNRS, CNES, LAM, Marseille, France
[4] Instituto de Astrofísica and Centro de Astroingeniería, Facultad de Física, Pontificia Universidad Católica de Chile, Casilla 306, Santiago 22, Chile
[5] Department of Physics and Astronomy, University of Southampton, Highfield SO17 1BJ, UK
[6] Dipartimento di Fisica e Astronomia, Università di Firenze, Via G. Sansone 1, 50019 Sesto Fiorentino, Firenze, Italy
[7] Osservatorio Astrofisico di Arcetri – INAF, 50125 Firenze, Italy
[8] Osservatorio Astronomico di Trieste – INAF, Via Tiepolo 11, 34143 Trieste, Italy
[9] INAF – Osservatorio Astronomico di Trieste, Via G. Tiepolo 11, 34124 Trieste, Italy
[10] Cavendish Laboratory, University of Cambridge, 19 J. J. Thomson Ave., Cambridge CB3 0HE, UK
[11] Istituto di Astrofisica e Planetologia Spaziali (INAF), Via del Fosso del Cavaliere 100, Roma 00133, Italy
[12] European Southern Observatory, Santiago, Chile
[13] Dipartimento di Fisica, Università di Roma La Sapienza, 00185 Roma, Italy
[14] Dipartimento di Fisica e Astronomia, Alma Mater Studiorum, Università degli Studi di Bologna, Via Gobetti 93/2, 40129 Bologna, Italy
[15] Osservatorio di Astrofisica e Scienza dello Spazio di Bologna – INAF, Via Gobetti 93/3, 40129 Bologna, Italy

Received 1 October 2019 / Accepted 24 January 2020

ABSTRACT

Context. The AGN bolometric correction is a key element for understanding black hole (BH) demographics and computing accurate BH accretion histories from AGN luminosities. However, current estimates still differ from each other by up to a factor of two to three, and rely on extrapolations at the lowest and highest luminosities.
Aims. Here we revisit this fundamental question by presenting general hard X-ray (K_X) and optical (K_O) bolometric corrections, computed by combining several AGN samples spanning the widest (about 7 dex) luminosity range ever used for this type of studies.
Methods. We analysed a total of ∼1000 type 1 and type 2 AGN for which we performed a dedicated SED-fitting.
Results. We provide a bolometric correction separately for type 1 and type 2 AGN; the two bolometric corrections agree in the overlapping luminosity range. Based on this we computed for the first time a universal bolometric correction for the whole AGN sample (both type 1 and type 2). We found that K_X is fairly constant at $\log(L_{BOL}/L_\odot) < 11$, while it increases up to about one order of magnitude at $\log(L_{BOL}/L_\odot) \sim 14.5$. A similar increasing trend has been observed when its dependence on either the Eddington ratio or the BH mass is considered, while no dependence on redshift up to $z \sim 3.5$ has been found. In contrast, the optical bolometric correction appears to be fairly constant (i.e. $K_O \sim 5$) regardless of the independent variable. We also verified that our bolometric corrections correctly predict the AGN bolometric luminosity functions. According to this analysis, our bolometric corrections can be applied to the whole AGN population in a wide range of luminosity and redshift.

Key words. black hole physics – galaxies: active – quasars: supermassive black holes – galaxies: evolution – galaxies: fundamental parameters – X-rays: galaxies

1. Introduction

To properly study the structure and evolution of active galactic nuclei (AGN) and understand how the observed local correlations between the super massive black hole (SMBH) mass and the host galaxy (Magorrian et al. 1998; Tremaine et al. 2002; Marconi & Hunt 2003; but see also Shankar et al. 2016, 2019) originate (in the AGN-galaxy coevolution scenarios), an accurate knowledge of the AGN internal mechanisms, physical properties, and then energetic budget of the AGN is necessary.

As a result, the bolometric luminosity, which is the total luminosity emitted at any wavelength by the AGN, becomes one of the key parameters that are to be known with the highest accuracy.

However, unless a wealth of multi-photometric data are available, it is necessary to use the so-called bolometric correction to derive the AGN bolometric luminosity. This is which is defined as the ratio between the bolometric luminosity and the luminosity in a given spectral band, that is, $K_{band} = L_{BOL}/L_{band}$.

Empirical bolometric corrections have a strong effect on our understanding of black hole (BH) demographics and AGN output, being widely adopted by the scientific community in both observational (e.g. to measure the fraction of total bolometric emission in AGN for a given band luminosity) and theoretical studies (e.g. in cosmological hydro-dynamical simulations to produce realistic synthetic catalogues of AGN, Koulouridis et al. 2018). Moreover, a correct knowledge of the bolometric

correction is fundamental for converting the AGN luminosity function into the accretion rate history (Salucci & Persic 1999; Ueda et al. 2003; Volonteri et al. 2003; Shankar et al. 2004; Marconi et al. 2004; Vittorini et al. 2005; La Franca et al. 2005; Aversa et al. 2015) and in turn deriving the local SMBHs (Soltan 1982), or more accurately, map the coeval growth of galaxies and their central SMBHs (Bongiorno et al. 2016; Aird et al. 2019).

The interest in this type of studies has been steadily increasing over time because larger AGN samples have become available. However, characterizing the AGN bolometric luminosity is a challenging problem for several reasons. First of all, we need to take the contamination from the host galaxy to the nuclear emission into account, which is a source of uncertainty particularly relevant for the AGN with lower luminosity. In addition, considering that the emission in different bands originates in diverse physical structures (a subparsec accretion disk in the UV-optical, a dusty parsec-scale torus in the IR and kiloparsec-scale relativistic jets in the radio), each spectral region varies with distinctive timescales. Another problem is the anisotropy of the AGN emission, which may depend on wavelength and may be peculiar to each specific source. Finally, given the multiwavelength feature of the AGN emission, observations from a variety of telescopes are necessary in order to build up complete and detailed spectral energy distributions (SEDs).

For these reasons, several attempts have been made in the past decades to accurately study the shape of the AGN SED (Sanders et al. 1989; Elvis et al. 1994; Richards et al. 2006). A key observational parameter is the optical-to-X-ray spectral index α_{ox}, defined as the slope of a power law connecting two regions of the SED: the UV (i.e., the accretion disc) and the X-rays (i.e., the so-called X-ray corona), and parametrized as $\alpha_{ox} = -\frac{\log(L_{2\,keV}/L_{2500\,Å})}{2.605}$ (Tananbaum et al. 1979). Some authors have investigated the evolution of the α_{OX} spectral index (see, e.g., Kelly et al. 2008; Vasudevan et al. 2009; Lusso et al. 2010; Marchese et al. 2012; Lusso & Risaliti 2017), which should provide an indication about the nature of the energy generation mechanism in AGN. Many of the authors reported that the UV-to-X-ray SED shows no significant dependence on redshift, while the primary dependence is on the UV luminosity (Vignali et al. 2003; Steffen et al. 2006; Lusso & Risaliti 2016). This supports a scenario in which the mechanism responsible for the nuclear emission of the AGN remains the same at any redshift, but correlates with the AGN luminosity: in particular, the ratio between the X-ray luminosity and the UV/optical luminosity decreases with increasing luminosity (see, e.g. Martocchia et al. 2017).

One of the first attempts to derive the bolometric correction was carried out by Elvis et al. (1994), who estimated the bolometric corrections in different bands using a mean energy distribution from a sample of 47 AGN, including the IR emission in the bolometric luminosity and therefore counting part of the emission twice. Shankar et al. (2004) gave a preliminary estimate of the hard X-ray bolometric correction, while Marconi et al. (2004) derived an estimate of the bolometric corrections in the optical B, soft and hard X-ray and IR bands, similarly to Hopkins et al. (2007) and Shen et al. (2020), who included the IR emission in the computation of the AGN total luminosity, however. Vasudevan & Fabian (2007) studied a sample of 54 X-ray bright ($L_X > 10^{43}$ erg s^{-1}) AGN, pointing out that particular classes of sources (as radio-loud, X-ray weak or narrow line Seyferts 1) might have different bolometric correction relations than the rest of the AGN population. Lusso et al. (2012) analyzed a sample of about 900 X-ray selected AGN deriving the bolometric corrections in the same bands as Marconi, separately for type 1 and type 2 sources, and valid for approximately three orders of luminosity. Runnoe et al. (2012a) sampled the optical band giving the bolometric corrections at three different wavelengths (1450 Å, 3500 Å and 4000 Å), while IR bolometric corrections were provided in Runnoe et al. (2012b). Krawczyk et al. (2013) focused on the characterization of the bolometric corrections of luminous broad-line AGN in a wide range of redshift ($0 < z < 6$). Very recently, Netzer (2019) provided simple power-law approximations of the bolometric corrections in the optical and hard X-ray bands, obtained by combining theoretical calculations of optically thick, geometrically thin accretion disks, and observational X-ray properties of AGN. Although all these works gave a good estimate of the AGN bolometric corrections in different bands, they were limited by the narrow range of luminosity sampled. This implies that for both high- and low-luminosity objects, most of the studies had to rely on extrapolations of the bolometric correction. Moreover, all of them, except for Lusso et al. (2012), focused on luminous, unobscured (type 1) sources, where the bolometric luminosity is much more easily measured because the SED is less strongly affected by obscuration and galaxy contamination than in type 2 sources.

We focus here on characterizing the hard X-ray ($K_X = L_{BOL}/L_X$) and the optical ($K_O = L_{BOL}/L_O$) bolometric corrections, considering a sample spanning the widest range of luminosity (about seven decades) so far that comprises both type 1 and type 2 sources, up to $z \sim 4$. Throughout the paper, L_X is the 2–10 keV intrinsic X-ray luminosity and L_O is the B-band 4400 Å luminosity.

The paper is organized as follows: in Sect. 2 we present the data sample, and Sect. 3 provides a detailed explanation of the SED-fitting method we used to separate the AGN and host galaxy emission components. In Sect. 4 we analyze the bolometric correction as a function of luminosity: Sect. 4.1 presents the results of the new hard X-ray bolometric correction for the type 1 and the type 2 sample separately, and then a general relation for the whole population; while Sect. 4.2 is dedicated to the optical bolometric correction for type 1 AGN. In Sect. 5 we study the bolometric correction as a function of redshift. Section 6 is dedicated to the study of the dependence of the bolometric corrections on the BH mass and Eddington ratio, while in Sect. 7 we derive the AGN unobscured bolometric luminosity function using the newly computed bolometric corrections. Finally, Sects. 8 and 9 present the discussion and our summary.

In what follows, we adopt a ΛCDM cosmology with $H_0 = 70$, $\Omega_m = 0.30$, $\Omega_\Lambda = 0.70$. All the uncertainties and spreads are quoted at 68% (1σ) confidence level, unless otherwise stated.

2. Data sample

We used a collection of ∼1000 sources belonging to five different AGN samples in order to cover the widest luminosity range (∼7 dex) ever sampled for this type of study (Fig. 1).

For this work we considered only radio-quiet AGN. We have therefore excluded from the analysis all sources with $\log L(1.4\,\mathrm{GHz}\ [\mathrm{W\,Hz^{-1}}]) > 26$ (see, e.g. Miller et al. 1990; La Franca et al. 2010).

2.1. Swift sample

The low-luminosity end is populated by the *Swift* sample, which consists of a collection of 21 type 1 (2×10^{41} erg s^{-1} $< L_X <$ 8×10^{45} erg s^{-1}) and 27 type 2 (3×10^{40} erg s^{-1} $< L_X < 3 \times$ 10^{44} erg s^{-1}) AGN at $z < 0.16$ from the *Swift*/BAT 70-month

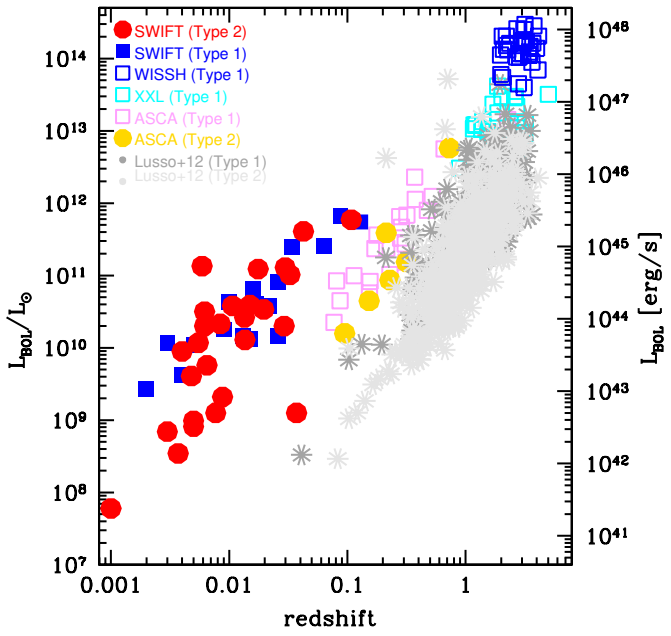

Fig. 1. Intrinsic X-ray luminosity in the 2–10 keV band as a function of the redshift of the *Swift* type 1 (blue filled squares) and type 2 (red filled circles) samples, the X-WISSH sample (blue open squares), the COSMOS type 1 (gray asterisks) and type 2 (light gray asterisks) sources, the ASCA type 1 (pink open squares) and type 2 (golden filled circles) objects and the XXL type 1 (cyan open squares) AGN.

catalog, which is considered one of the most complete hard X-ray surveys, containing about 1200 hard X-ray objects in the 14–195 keV band, of which about 700 are classified as AGN sources (Baumgartner et al. 2013). For these AGN, the intrinsic hard X-ray luminosity is provided by Ricci et al. (2017a). We remark that with the term type 1 AGN we define the targets that show broad emission lines in the optical spectra, and we refer to type 2 AGN as those AGN without (Seyfert 2) or with weak (intermediate 1.8–1.9) evidence of the broad line region, or even without any lines at all in their optical spectra. The *Swift* type 2 AGN belong to an original sample of 41 AGN, for which our group obtained near-IR (NIR) spectroscopic observations using ISAAC and X-shooter at the Very Large Telescope (VLT), and the LBT Utility Camera in the Infrared (LUCI) at the Large Binocular Telescope (LBT; Onori et al. 2017a). Six additional sources with data from the literature have been added at a second time. In this total sample of 47 AGN, a fraction of ∼30% showed faint broad emission lines after deep NIR spectroscopy that allowed us to estimate their BH mass, $M_{\rm BH}$ (see Onori et al. 2017b) using the BH mass virial estimator calibrated by Ricci et al. (2017b).

The *Swift* type 1 AGN belong to an original sample of 33 sources that were presented in Ricci et al. (2017c) and were included in the *Swift*/BAT 70-month catalog, whose $M_{\rm BH}$ were measured via reverberation mapping techniques, and for which reliable bulge classification is available (Ho & Kim 2014). This sample has been adopted by Ricci et al. (2017b) to calibrate a virial BH mass estimator that can be used to measure $M_{\rm BH}$ of low-luminosity obscured AGN. According to Onori et al. (2017b) and Ricci et al. (2017c), the local type 1 and type 2 sources can be considered representative of the AGN populations that are included in the *Swift*/BAT catalog. As shown in Fig. 1, this sample allows us to probe the lowest luminosity range of our entire dataset.

In order to estimate the physical properties of the *Swift* AGN sample, a multiwavelength photometric dataset was collected. We removed two radio loud (RL) sources from the original *Swift*/BAT 70-month catalog and considered only the data whose photometric aperture was representative of the flux of the entire galaxy. We then collected photometric data for a total of 36 bands, using the NASA/IPAC Extragalactic Database (NED)[1] and other public catalogs: far- and near-UV data are from observations obtained with the Galaxy Evolution Explorer (GALEX) observations (GildePaz et al. 2007); U, B, V, R and I bands are taken from the Atlas of galaxies by de Vaucouleurs et al. (1991) or from the Sloan Digital Sky Survey (SDSS) DR12[2]; the NIR J, H, and K bands from the Two Micron All Sky Survey (2MASS)[3]; data at 3 μm, 4.5 μm, 12 μm and 22 μm are from the Wide-field Infrared Survey Explorer (WISE)[4]; data at 12 μm, 25 μm, 60 μm and 100 μm are from the Infrared Astronomical Satellite (IRAS) and from the IRAS Revised Bright Galaxy Sample by Sanders et al. (2003); 120 μm, 150 μm, 170 μm, 180 μm and 200 μm- band are from ISOPHOT (Spinoglio et al. 2002); finally, FIR data at 250 μm, 350 μm and 500 μm are from *Herschel* (Shimizu et al. 2016) or the Balloon-borne Large Aperture Submillimiter Telescope (BLAST; Wiebe et al. 2009). We discarded the sources for which the data were not sufficient to guarantee a good photometric coverage. In particular, we included only the objects for which (1) we have more than three bands for each region of the spectrum, that is, UV/optical, NIR and mid-IR (MIR); and (2) each photometric value has a signal-to-noise ratio $S/N > 5$. For this reason, 20 of the 46 type 2 sources and 12 of the 32 type 1 sources were excluded from our analysis. Therefore the local sample of *Swift* AGN includes 26 type 2 and 20 type 1 AGN. This selection could induce a bias in the SEDs of the sources we analyzed. We investigated this possibility by studying the X-ray-to-MIR ratio distribution (using the WISE W1 band, whose value is available for all the objects). The sample of the excluded sources (OUT sample) shows an average X-ray/MIR that is 0.2 dex higher than that of the included sources (IN sample) at 2.5σ, while in the total sample the X-ray/MIR is 0.09 dex higher than that of the IN sample. However, as discussed below, this bias has negligible effects on the final derived bolometric correction relations and on the main conclusions of this paper (see Sect. 4.1).

2.2. X-WISSH sample

At the brightest end, we started from the WIse Selected Hyperluminous (WISSH) sample (see Bischetti et al. 2017), which is composed of 86 hyperluminous ($L_{\rm BOL} > 2 \times 10^{47}$ erg s^{-1}) type 1 AGN in the redshift range $2 < z < 4$, detected in the MIR by WISE. Of the 86 sources, 41 have been observed in the X-rays by XMM or *Chandra* (see Martocchia et al. 2017). Six X-ray undetected and two RL sources were excluded from our analysis, resulting in a final X-WISSH sample of 33 type 1 AGN. For all of them, a wide photometric coverage (from the X-ray to the MIR) is available.

2.3. COSMOS sample

This sample includes 369 type 1 and 484 type 2 sources from the XMM-COSMOS catalog that were studied by

[1] https://ned.ipac.caltech.edu/
[2] https://www.sdss.org/dr12/
[3] https://irsa.ipac.caltech.edu/Missions/2mass.html
[4] https://irsa.ipac.caltech.edu/Missions/wise.html

Lusso et al. (2012, hereafter L12), in the redshift range $0.1 < z < 4$. The average hard X-ray luminosity is $L_X \sim 10^{44}$ erg s^{-1}. From the sample presented in L12, we rejected 4 RL type 1 and 3 RL type 2 sources. The original type 2 sample in L12 was composed of 488 AGN, but one source had an incorrect spectroscopic classification and was eventually classified as an inactive galaxy. The intrinsic hard X-ray luminosities of the sources are published in L12, and we refer to that work for the derivation of their physical properties.

2.4. ASCA sample

This sample belongs to the ASCA Medium Sensitivity Survey in the northern sky (AMSSn) sample that was analyzed by Akiyama et al. (2003). We used all the AGN sources for which good photometric data were available (see the criteria adopted for the *Swift* sample). Their photometry has been obtained by cross-correlating data from the SDSS, the 2MASS survey and WISE. The final ASCA sample, after removing one type 1 RL AGN, contains 22 type 1 and 6 type 2 sources, up to $z \sim 2.3$. The original X-ray luminosity published in Table 3 of Akiyama et al. (2003), was rescaled according to our adopted values of the cosmological parameters.

2.5. XXL sample

Finally, we used a subsample of AGN from the XXL-N survey (Pierre et al. 2016). From the 8445 point-like X-ray sources presented by Liu et al. (2016), we selected AGN with 2–10 keV photon counts greater than 50. From these, we chose those with high bolometric luminosities ($L_{\rm BOL} > 10^{46.5}$ erg s^{-1}, as listed in their Table 2) in order to achieve better statistical significance in the highest luminosity regime just below the one probed by the X-WISSH sample. We removed 6 RL sources and therefore the final XXL sample consists of 31 type 1 AGN in the redshift range $0.9 < z < 5$.

In all the above samples the 2–10 keV intrinsic X-ray luminosities derived from X-ray spectral fitting were used when available. Otherwise, they were rescaled by assuming a typical common $\Gamma = 1.8$ photon index value.

We stress that all the described samples except for the X-WISSH sample are X-ray selected, which could in principle introduce a bias in the estimate of the bolometric correction. However, we show in Sect. 4.1 that this effect can be considered to be negligible.

3. Spectral energy distribution

In this section we focus on the SED characterization and on the consequent derivation of the main physical properties (in particular the bolometric luminosity) of the sources belonging to the *Swift*, X-WISSH, ASCA and XXL samples. The properties of the COSMOS sample were taken from L12, who used an SED-fitting method similar to the one adopted in this paper (see Sect. 3.2).

3.1. SED fitting

The SED fitting procedure is based on a modified version of the code described in Duras et al. (2017, hereafter D17). The observed SED of each source is the result of different components produced by the nuclear engine and the stellar light (e.g., Bongiorno et al. 2012; Berta et al. 2016; Calistro Rivera et al. 2016). The nuclear emission produces two bumps in the UV and NIR regimes that create a dip at around 1 μm (Sanders et al. 1989; Elvis et al. 1994; Richards et al. 2006). The UV bump is due to thermal emission from the accretion disk (Czerny & Elvis 1987), and the NIR bump to the reemission at longer wavelengths of the intrinsic primary radiation that is absorbed by hot dusty clouds in the torus. In the same way, the stellar light produces a direct UV/optical emission (mainly due to hot stars) and a MIR-FIR component (ascribed to its reprocessing by the cold dust located on galactic scales). How much these two components contribute to the global SED depends on a number of factors, the most important ones being their relative luminosity and the level of obscuration that affects each of them.

In D17 the fit was performed with three emission components:

1. the accretion disk plus torus emission (using a combination of models by Feltre et al. (2012) and Stalevski et al. 2016),
2. the cold dust emission connected to the galactic star formation activity (modeled as a modified blackbody),
3. an additional component in the MIR, representing warmer dust in the vicinity of the nucleus (described by a simple blackbody).

We here used an improved version of the code described in D17 in order to also take sources with low contribution from the nuclear engine into account, using the photometric information in the X-ray band. To do this, (a) we added an additional component, that is, the UV-optical stellar emission from the host galaxy; (b) and the optical-to-MIR AGN SED was modeled starting from the hard X-ray normalized templates by Silva et al. (2004).

(a) The galaxy emission component was not included in D17 for the study of type 1 WISSH AGN because the UV galactic light is completely outshone by the AGN emission for such bright unobscured sources. We here added a galaxy component to the three emission components that were used in D17. The galaxy emission is produced by the integrated light of diverse stellar populations characterized by distinct star formation histories (SFHs). We generated a library of synthetic spectra, using the stellar population synthesis models of Bruzual & Charlot (2003). We assumed a Chabrier (2003) initial mass function, building 10 declining SFHs as a function of the e-folding time and the age of the galaxy (see, e.g., Bongiorno et al. 2012). For all the galactic templates we took the effect of dust extinction inside the galaxy into account, choosing as reddening curve the Calzetti's law (Calzetti et al. 2000). The final library of galaxy templates we used consists of about 900 templates with extinction in the range $0 \leq E(B-V) \leq 0.5$.

(b) In type 1 unobscured sources, the AGN component dominates the optical and IR bands compared to the host galaxy emission; in contrast, in type 2 obscured AGN, the SED is characterized by an optical continuum dominated by the host galaxy emission, while the AGN component is mainly relevant at IR wavelengths. To model the emission from type 2 AGN we adopted the AGN SEDs by Silva et al. (2004), which were derived from a sample of 33 Seyfert galaxies properly corrected for any galaxy nuclear contribution. They are available in four intervals of X-ray absorption: $N_{\rm H} < 10^{22}$ cm^{-2} for Seyfert 1 (Sy1), $10^{22} < N_{\rm H} < 10^{23}$ cm^{-2}, $10^{23} < N_{\rm H} < 10^{24}$ cm^{-2} and $N_H > 10^{24}$ cm^{-2} for Seyfert 2 sources (Sy2). Being hard X-ray normalized SEDs, they are able to provide the AGN optical-to-MIR component when good-quality hard X-ray photometric data (corrected for absorption, see Ricci et al. 2017a) are available, as in the case for our sources. As shown by Silva et al. (2004), all the AGN X-ray normalized SEDs can be considered quite identical

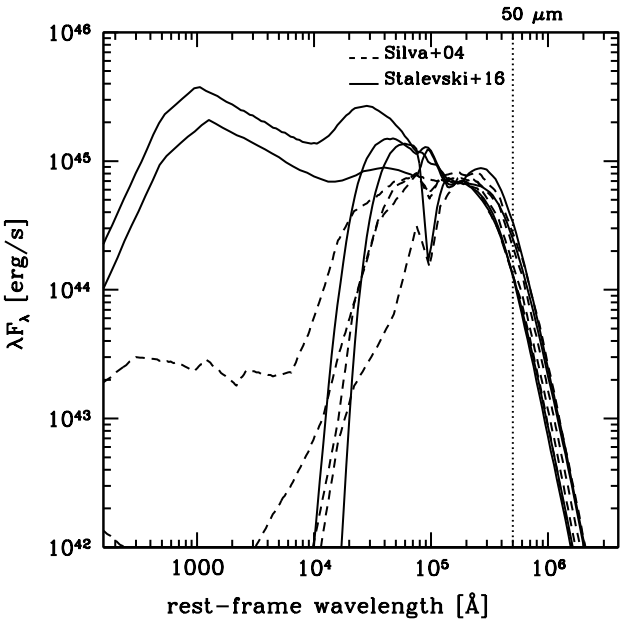

Fig. 2. Examples of UV-to-IR AGN templates with different levels of absorption from Silva et al. (2004) and Stalevski et al. (2016). The vertical dotted line at ~50 μm shows the position of the pivotal photometric point derived from the X-ray luminosity, where the AGN templates are very similar.

above 40 μm (see Fig. 2), with a spread of about 0.1 dex. Assuming an average value of the SEDs at 50 μm, we therefore converted the hard X-ray photometry into a virtual pivotal photometric, to be fit only by the AGN templates (see Fig. 3). Aware of this assumption, to overcome the limitation of having only four AGN templates, and in the meantime to better reproduce the spectral emission of either very luminous type 1 or very low luminous type 2 AGN, we enriched the library with the models by Stalevski et al. (2016) used in D17.

To summarize, our emission model ($f_{\rm model}$) includes four emission components:

$$f_{\rm model} = A f_{\rm AGN} + B f_{\rm GAL} + C f_{\rm CD} + D f_{\rm ME}, \quad (1)$$

where $f_{\rm AGN}$ represents the emission coming from the active nucleus, both direct and reprocessed by the dusty torus, $f_{\rm GAL}$ is the emission from the stars, $f_{\rm CD}$ accounts for the FIR emission due to the reprocessed flux by cold dust and is modeled as a modified blackbody, and $f_{\rm ME}$ is any possible excess MIR component, modeled as a simple blackbody. Finally, A, B, C and D are the relative normalizations. The fitting procedure allows us to determine through a χ^2 minimization the combination of templates that best describes the observed SED and their relative contributions.

3.2. SED results

Based on the final SED best-fit models, the intrinsic AGN bolometric luminosity of the type 1 AGN sources was derived by integrating the AGN emission component in the range 20 Å–1 μm. As L12, we neglected the IR emission to avoid counting the UV/optical photons twice that are reprocessed by the dust (for a different approach see Hopkins et al. 2007, who instead included this component in the estimation of the total emitted SEDs due to the AGN activity). It is worth noting that the values of the bolometric luminosity published in D17 for the nine

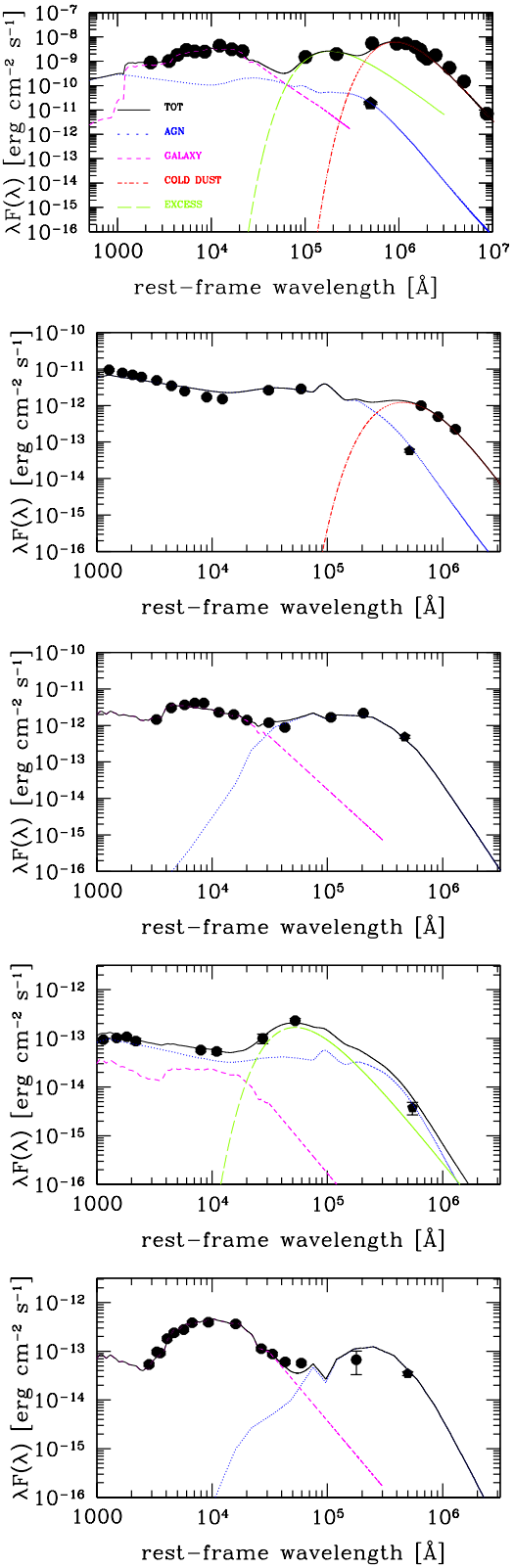

Fig. 3. Example of SED fitting results. *From top to bottom*: one type 2 source from the *Swift* sample, one type 1 from the X-WISSH sample, one type 2 from the ASCA sample, one type 1 from the XXL sample and one type 2 from the COSMOS sample. The AGN, galaxy, cold dust and excess emission components are shown in different colors and line types (as stated in the legend of the first figure in the *top panel*). Black circles are the photometric points of the source. The virtual AGN pivotal photometric point at 50 μm, derived from the hard X-ray data, is shown as the black pentagon (see text for details).

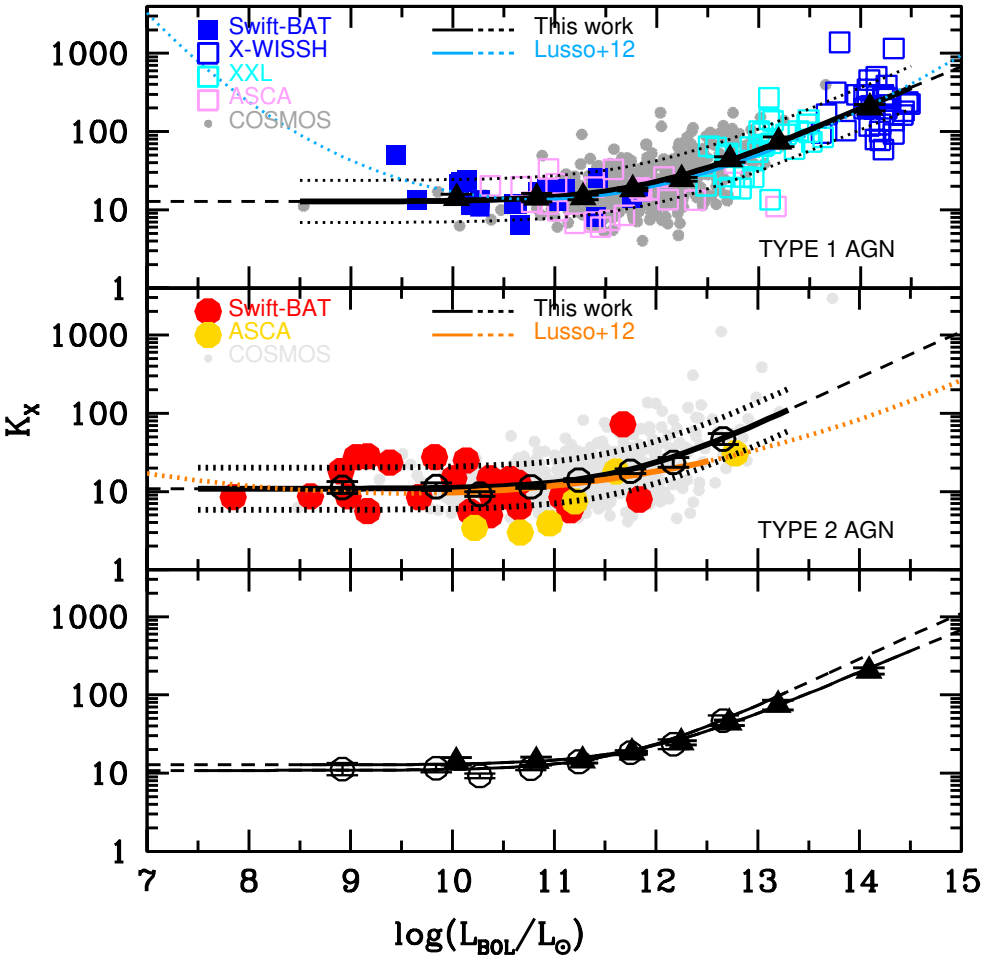

Fig. 4. Hard X-ray bolometric correction in the 2–10 keV band as a function of the bolometric luminosity for type 1 (*upper panel*) and type 2 (*central panel*) AGN. Symbols are as in the legend. Black filled triangles and open circles show the average values for type 1 and type 2 sources, respectively (directly compared in the *lower panel*), in bins of bolometric luminosity. The black solid and dashed lines show our best-fit relations and their extrapolations according to Eq. (2).

X-WISSH sources with *Herschel* coverage (in common with this work) are almost identical (within few percent) to those obtained using our modified version of the SED-fitting code, that is, including the X-ray photometric information.

Type 2 AGN emission in the UV/optical bands is known to be more affected by the host galaxy than type 1 AGN. In this case we followed the approach by Pozzi et al. (2007) to compute the bolometric luminosity by integrating the AGN template in the range 1 μm–1000 μm and simply rescaling the result for a factor 1.9 (see also Vasudevan et al. 2010). If instead the X-ray luminosity is included (as was done for the XMM-COSMOS sources by L12), this factor is reduced to ∼1.7 (Pozzi et al. 2007). This correction accounts for the geometry of the torus and its orientation. It is indeed related to the covering factor f (which represents the fraction of the primary optical-UV radiation intercepted by the torus) and to the anisotropy of the IR emission, function of the viewing angle. We verified that when we applied this method to the type 1 sources, the resulting bolometric luminosities are consistent (within 8%) with those obtained by the direct integration of the UV-to-NIR AGN emission.

We verified that the SED-fitting method described above provides results similar to those obtained by L12 for the COSMOS sample. In a random sample of ten type 1 and ten type 2 COSMOS AGN, the bolometric luminosities estimated using our SED fitting agree with L12 within 0.04 dex. Such a small discrepancy was indeed expected, because the bolometric luminosity is the area below the AGN emission template and therefore slightly dependends on the chosen combination of models for the total emission.

The values of the derived bolometric luminosity for the *Swift*, X-WISSH, ASCA and XXL samples are reported in Tables A.1–A.4.

4. Bolometric correction as a function of luminosity

The bolometric correction is by definition the ratio between the AGN bolometric luminosity and the luminosity computed in a specific band. It is a quantity of primary importance in astronomy, because it allows us to obtain an estimate of the AGN bolometric luminosity when a complete SED is not available.

4.1. Hard X-ray bolometric correction

As a first step, we studied the dependence of the AGN hard X-ray bolometric correction on the bolometric luminosity, that is, $K_X(L_{BOL})$. In Fig. 4 we show K_X as a function of L_{BOL} for all type 1 sources (upper panel) and type 2 (central panel) sources. Black filled triangles and open circles represent the average of the bolometric corrections computed in bolometric luminosity (not overlapping) bins, for type 1 and type 2 AGN respectively. The light blue continuous line in the upper panel shows the relation found by L12 for their type 1 AGN from the COSMOS sample, while the orange continuous line in the central panel shows the relation found by L12 for their type 2 COSMOS sample; the dotted lines mark the extrapolation of these relations out of the range covered by the L12 data. The X-WISSH sample and the *Swift* sample clearly cover a range in luminosity that has never been studied before. At high luminosities, as has been

Table 1. Best-fit parameters for the hard X-ray bolometric correction as a function of either the bolometric luminosity (Eq. (2)) or the hard X-ray luminosity (Eq. (3)).

	a	b	c	Spread [dex]
		$K_X(L_{BOL})$		
Type 1	12.76 ± 0.13	12.15 ± 0.01	18.78 ± 0.14	0.26
Type 2	10.85 ± 0.08	11.90 ± 0.01	19.93 ± 0.29	0.27
General	10.96 ± 0.06	11.93 ± 0.01	17.79 ± 0.10	0.27
		$K_X(L_X)$		
General	15.33 ± 0.06	11.48 ± 0.01	16.20 ± 0.16	0.37

Notes. The luminosities are expressed in solar units.

pointed out in M17, the X-WISSH data follow the extrapolation of the L12 relation at high luminosities fairly well, while at low luminosities the *Swift* sample data favor a flatter or constant relation at $\log(L_{BOL}/L_\odot) < 11$.

We fit the type 1 and type 2 samples separately, using a least-square method, with the following relation:

$$K_X(L_{BOL}) = a\left[1 + \left(\frac{\log(L_{BOL}/L_\odot)}{b}\right)^c\right]. \quad (2)$$

The best-fit relations for type 1 and type 2 AGN are shown in Fig. 4 as a black continuous line, and the best-fit parameters, along with the intrinsic average spread of the data (≃0.27 dex), are listed in Table 1. The values of the spread for the type 1 and the type 2 samples are quite similar and agree well with those found by L12 (∼0.25 for both populations). Figure 5 shows that the spread is almost constant throughout the whole luminosity range probed by the data.

At low luminosities (in the range $7.5 < \log(L_{BOL}/L_\odot) < 11$) the bolometric correction has a constant value, while it increases at $\log(L_{BOL}/L_\odot) > 11$: for type 1 sources, our solution is very similar to the relation found by L12 for their type 1 AGN; in contrast, for type 2 sources, at $\log(L_{BOL}/L_\odot) > 12.5$ it is systematically higher than the one by L12. This might be due to the new functional form we used, which allows a better representation of the data sample, and to the fact that the fitting procedure in L12 has been carried out on binned data, while we performed the fits considering the whole dataset.

The lower panel of Fig. 4 shows that where the average values of $K_X(L_{BOL})$ of type 2 sources (open black circles) are compared with those for type 1 sources (filled black squares), type 1 and type 2 AGN seem to share the same general bolometric correction relation. Moreover, as we mentioned above, the two samples have almost the same value of the spread (0.27 dex). We thus investigated whether a general bolometric correction relation, for type 1 and type 2 sources, was consistent with the data. In Fig. 6 we show the K_X as a function of L_{BOL} for the whole sample of type 1 and type 2 AGN. Black filled hexagons represent the average bolometric corrections computed in bolometric luminosity bins for the whole sample. Our best-fit relation is shown as a black line, while the two black dotted lines correspond to the 1σ spread of the sample. We found that this general $K_X(L_{BOL})$ relation can be considered statistically representative of the whole AGN population. Indeed, it is not rejected by the χ^2 test when it is applied on the type 1 and type 2 samples separately ($P(>\chi^2) = 0.45$ in both cases); because the values of the spread are very similar for the type 1, type 2 sources and the whole sample, an average spread of ∼0.27 dex was assumed

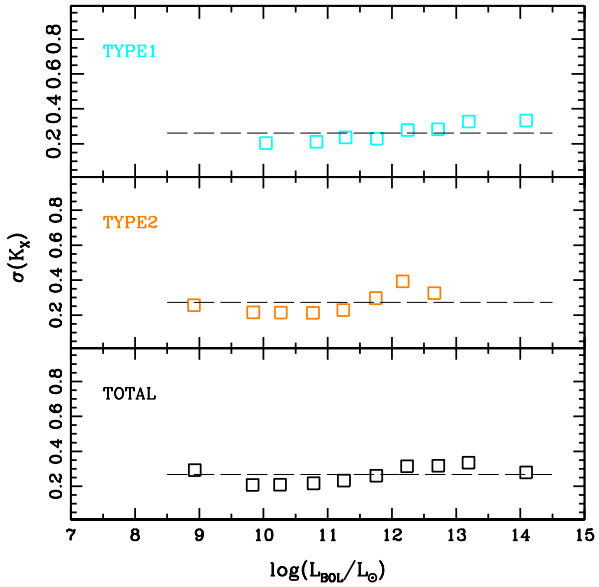

Fig. 5. Intrinsic spread in bins of bolometric luminosity for the X-bolometric correction of type 1, type 2, and the whole AGN sample. Dashed black lines show the average value.

(see Fig. 5) when we computed the χ^2 test. This result has been pointed out by L12, who argued that the bolometric correction relation for the type 2 sources seems to be the natural extension at lower luminosities of the one for the type 1 sources. Based on the inclusion of the low- and high-luminosity samples used in this work, we were then been able to derive a universal bolometric correction relation that is valid for the entire X-ray selected AGN population and over the largest (7 dex) luminosity range ever probed. As we mentioned in Sect. 2, the X-WISSH sample alone is not X-ray selected, and this might introduce a bias in the resulting bolometric correction. To determine whether this might cause a significant difference in the final result, we performed a new fit excluding the X-WISSH sources from the total sample, thus minimizing possible biases arising from different selection methods. The difference between the results is negligible: on average 0.01 dex at the highest luminosities. This shows that including the X-WISSH sources allowed us to reduce the uncertainties at the highest luminosities ($\log(L_{BOL}/L_\odot) > 13.5$) and to extend the validity of the bolometric correction to this extreme regime.

In Fig. 6 the bolometric corrections by L12 for their COSMOS samples of type 1 and type 2 AGN, are shown as cyan and orange lines, respectively. Our result agrees well with these relations, when it is compared within the luminosity range of the COSMOS data used by L12 ($11 < \log(L_{BOL}/L_\odot) < 13$). Conversely, as previously found by L12, at $\log(L_{BOL}/L_\odot) \sim 11.5$ the Marconi et al. (2004, purple line) and Hopkins et al. (2007, magenta line) bolometric corrections are about 0.20–0.25 dex higher than ours. While we directly computed the bolometric corrections for each object, Marconi et al. (2004) obtained them by assuming an α_{OX} relation that was certainly less accurate than is currently available; this might justify the discrepancy (although surprisingly small) with our relation. Hopkins et al. (2007) included the IR contribution in the estimate of the bolometric luminosity, because they were interested in characterizing the observed SED of the AGN.

The majority of the studies that focused on BH accretion and demography (as mentioned in the Introduction) have used the bolometric correction as a function of the luminosity in a

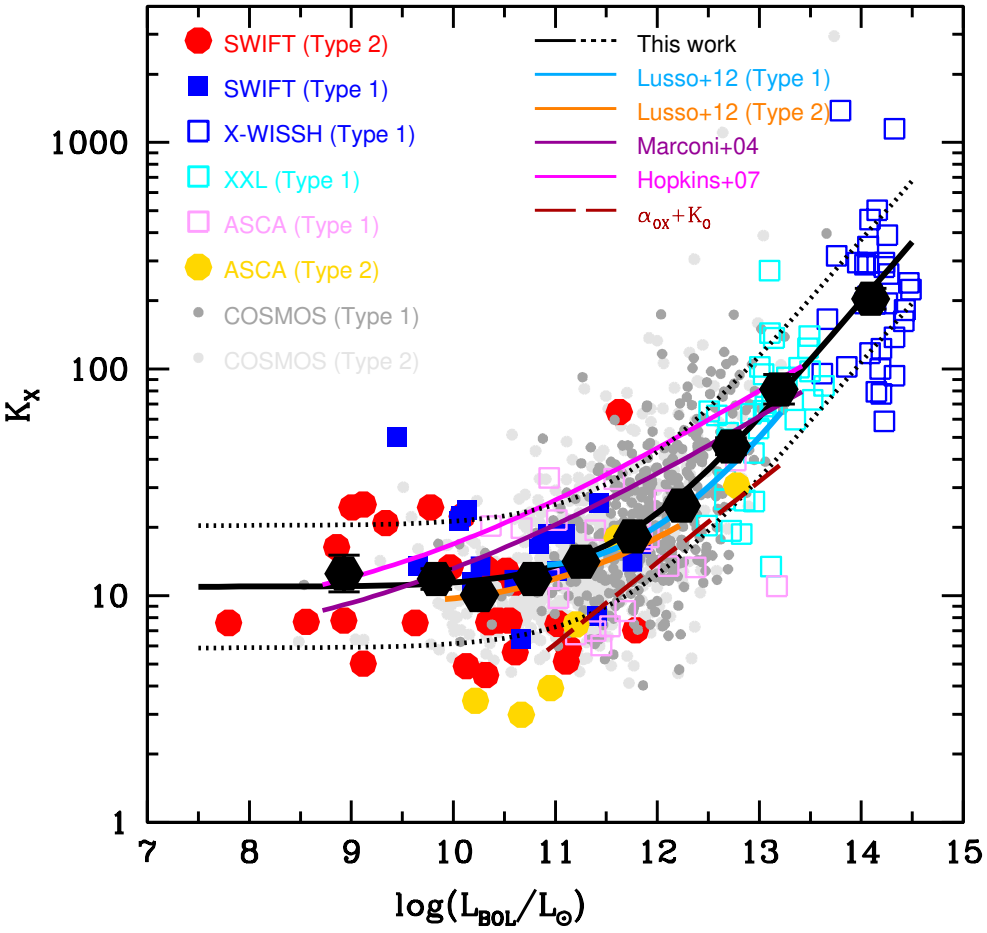

Fig. 6. General hard X-ray bolometric correction in the 2–10 keV band as a function of the bolometric correction for type 1 and type 2 AGN. Symbols are the same as in Fig. 4. Black hexagons are the average bolometric correction values, in bins of bolometric luminosity. The black solid line is our best-fit solution; the brown solid line is the analytical prediction obtained by assuming the relation between the X-ray luminosity and the optical luminosity by Lusso & Risaliti (2016) and the optical bolometric correction by L12. See text and Table 1 for details.

specific band. Although it is possible to numerically convert the $K_X(L_{BOL})$ into a relation in which the bolometric correction depends on the X-ray luminosity, we directly fit this relation using the following equation:

$$K_X(L_X) = a\left[1 + \left(\frac{\log(L_X/L_\odot)}{b}\right)^c\right]. \quad (3)$$

The parameters and the relative spread are shown in Table 1. As discussed in Sect. 2, the 46 AGN of the *Swift* sample are affected by a small bias in favor of sources that on average have an X/MIR that is about 0.1 dex larger than the parent sample. We have verified that this bias is negligible: the fits differ by only 0.025 dex once the L_{BOL} values of the *Swift* AGN are reduced by 0.1 dex.

The $K_X(L_X)$ relation provides on average the same X bolometric correction as the $K_X(L_{BOL})$ one, with differences within 0.2 dex in the range $8 < \log(L_{BOL}/L_\odot) < 13$ (see also the discussion on the resulting bolometric luminosity function in Sect. 7). However, because the spread (~0.37) of this relation is higher, we strongly encourage adopting the bolometric correction relation as a function of the bolometric luminosity, that is, Eq. (2).

4.2. Optical bolometric correction

In addition to the hard X-ray bolometric correction we also studied the dependence of the optical (specifically in the *B* band, at 4400 Å) bolometric correction on the bolometric luminosity. We measured the optical luminosity from the photometric point at 4400 Å rather than from the best AGN model provided by the SED-fitting procedure. In this way, the optical and bolometric luminosities are independent of each other and no artificial relation between them is introduced. Considering that for type 2 obscured AGN the optical emission is mostly dominated by the host galaxy, we included only type 1 sources of each sample in this specific analysis.

In Fig. 7 we show the K_O as a function of L_{BOL}. Black hexagons represent the average of the bolometric correction in bins of bolometric luminosity. As was found by L12 (whose relation is reported for comparison as a light blue line), the optical bolometric correction does not significantly depend on the bolometric luminosity. The Pearson linear correlation test gives a coefficient R equal to ~0.069, corresponding to a probability of 14% to be linearly related. We then fit the data with a constant value, using the relation:

$$K_O(L_{BOL}) = k. \quad (4)$$

Our best-fit relation, $K_O(L_{BOL}) \sim 5.13$, is shown as a black solid line, while the 1 σ spread of the sample (~0.26 dex) is marked with the two dotted lines (see Table 2). The values of the bolometric correction at the lowest bolometric luminosities ($\log(L_{BOL}/L_\odot) < 11$) are about a factor of 2 lower than the rest of the sample. As suggested by L12, this behavior might be ascribed either to a simple statistical fluctuation, due to the small number of low-luminosity sources, or to the fact that in this range the *B*-band luminosities might be influenced by the contribution of the host galaxy. However, the inclusion or exclusion of these objects does not significantly affect the average value of the optical bolometric correction.

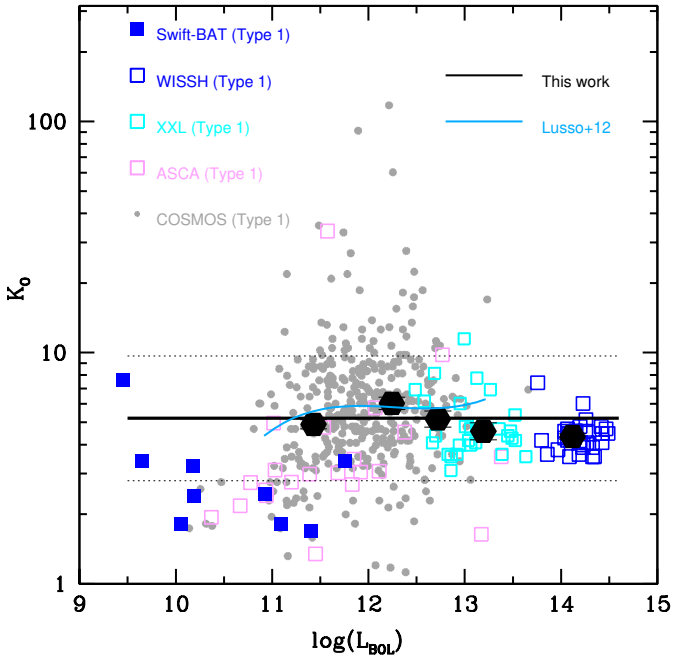

Fig. 7. Optical bolometric correction computed at 4400 Å for type 1 sources. The black solid line is our best-fit solution. See text and Table 2 for details.

Table 2. Best-fit parameters for the optical bolometric correction as a function of either the bolometric luminosity (Eq. (5)) or the optical luminosity.

	k	Spread [dex]
$K_O(L_{BOL})$	5.13 ± 0.10	0.26
$K_O(L_O)$	5.18 ± 0.12	0.27

We also studied the dependence of the optical bolometric correction on the optical luminosity, $K_O(L_O)$. We fit the data with a constant value, using the relation:

$$K_O(L_O) = k, \quad (5)$$

where $k = 5.18 \pm 0.13$, with a spread of ~0.27 dex (see Table 2). The very similar intrinsic spread means that these two relations could be used without distinction.

5. Bolometric correction as a function of redshift

We investigated the redshift dependence of the hard X-ray bolometric correction relation. To this end, we computed the normalized bolometric correction by dividing the X-ray bolometric correction of each source by the average value as derived by our best-fit relation (Eq. (2)). The normalized values (black hexagons) and the best-fit (dashed line) are shown in Fig. 8 (top panel), and suggest no trend with redshift. As a second test, we divided the whole sample into five ranges of hard X-ray luminosity (bottom panel). Again, black hexagons are the average values of bolometric correction in bins of redshift, and the black dashed lines represent the average value of the bolometric correction of the sample in each range of L_X. In this case we also find that in none of the analyzed luminosity ranges there is a hint of dependence on redshift.

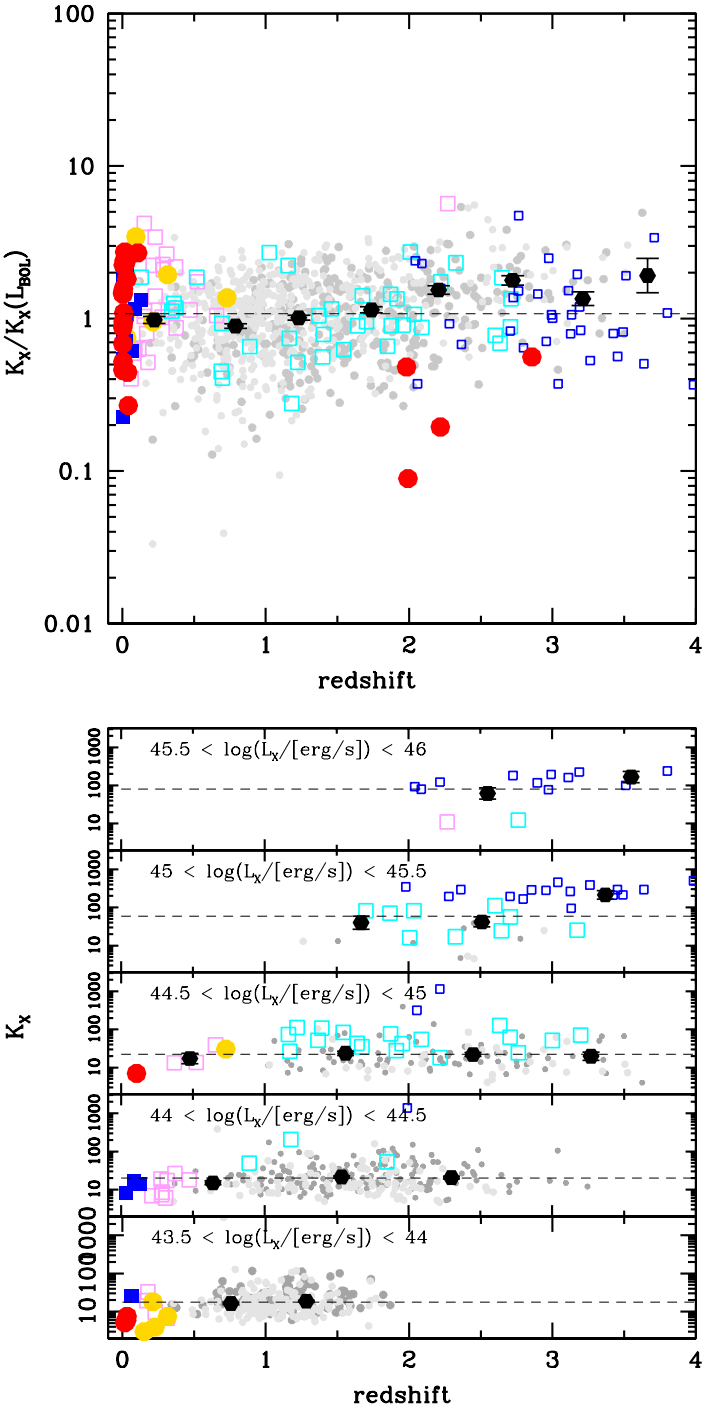

Fig. 8. Hard X-ray bolometric correction as a function of redshift. In the *top panel*, the normalized bolometric correction has been obtained by dividing K_X for the corresponding bolometric correction given by Eq. (2). *Bottom panel*: K_X as a function of redshift in five ranges of hard X-ray luminosity. Black hexagons are the average values of K_X computed in bins of redshift and the dashed line is the average K_X of the whole sample within the entire redshift range. Symbols are the same as in Fig. 6.

6. Bolometric correction as a function of Eddington ratio and BH mass

Many authors have found a correlation (although with a huge scatter) between the bolometric correction and either the Eddington ratio ($\lambda_{EDD} = L_{BOL}/L_{EDD}$) or the BH mass (e.g.,

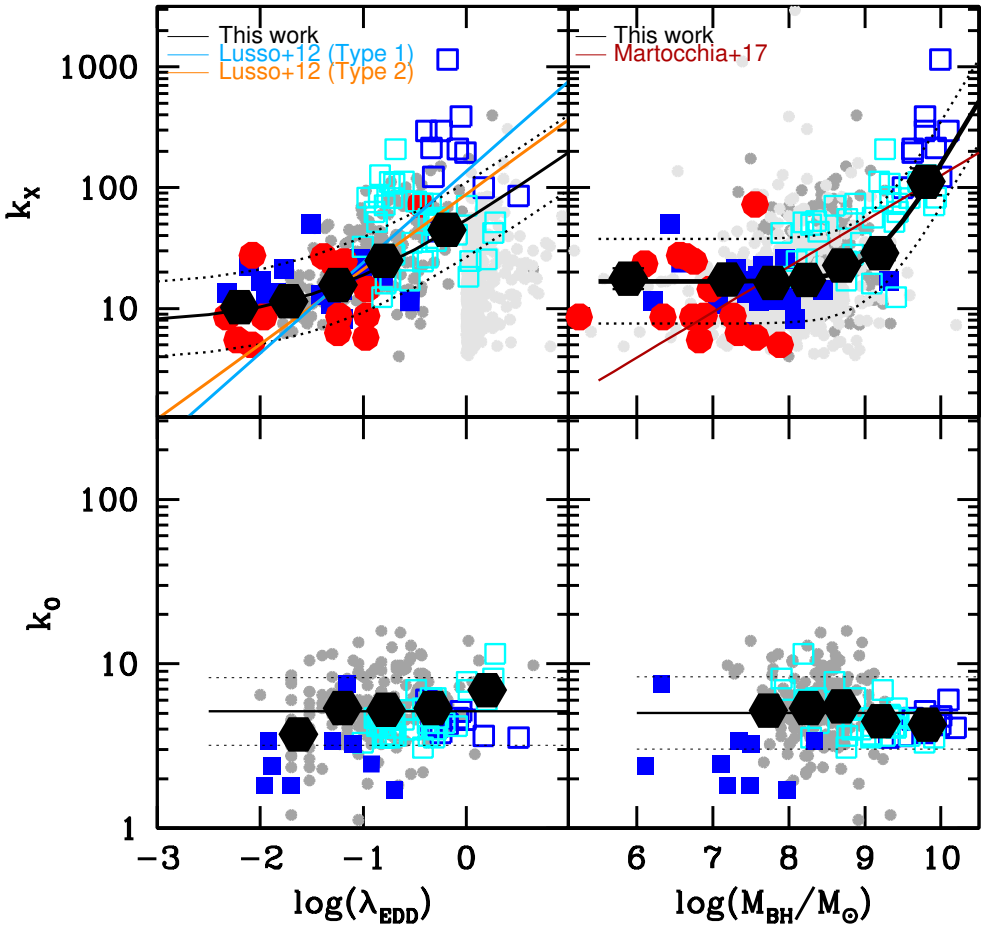

Fig. 9. *Upper panels*: hard X-ray bolometric correction as a function of the Eddington ratio (*left*) and of the BH mass (*right*). *Lower panels*: optical bolometric correction as a function of the Eddington ratio (*left*) and of the BH mass (*right*). Black solid lines show our best-fit relations. Symbols are the same as in Fig. 6.

Vasudevan & Fabian 2007; Vasudevan et al. 2009; Lusso et al. 2010). We studied these dependencies using the same samples as presented above, but limited to the 745 objects for which the M_{BH} was measured: 21 type 1 and 15 type 2 sources by Onori et al. (2017b) for the *Swift*/BAT sample (whose M_{BH} has been derived from reverberation mapping techniques and deep NIR spectroscopy, see Sect. 2); 11 WISSH type 1 sources (with Hβ-based virial masses provided in Vietri et al. 2018); 661 COSMOS AGN by L12 (with masses obtained from virial estimators for the type 1 AGN and from M_{BH}–M_* relations plus morphological information for the type 2 subsample); and the 37 XXL sources (whose virial masses are estimated from Hβ, Mg$_{II}$, and C$_{IV}$ broad lines). To have measurements that are as homogeneous as possible, we rescaled the BH mass values of the *Swift* sample by assuming the same virial factor (f = 5.5) as for the other samples (instead of f = 4.31 as in Ricci et al. 2017c). In the COSMOS type 2 sample, the BH masses have been derived by L12 using the M_{BH}–M_{bulge} relation by Häring & Rix (2004) after correcting for the bulge-to-total mass ratio. We caution the reader that this last method is different from the method that was used for all the other samples we studied. This might therefore introduce a bias in the M_{BH} estimates. In the upper panels of Fig. 9 the hard X-ray bolometric correction is shown as a function of the λ_{EDD} (left panel) and the M_{BH} (right panel). Black hexagons are the average values of the hard X-ray bolometric correction computed in bins of λ_{EDD} and M_{BH}. Figure 9 shows that the bolometric correction as a function of the BH mass is only applicable in the range $\lambda_{EDD} > 10^{-2}$ because our AGN sample does not cover BHs that accrete at lower values of the Eddington ratio. In the upper left panel, the relations published in L12 for their type 1 and type 2 COSMOS AGN are reported as light blue and orange straight lines. As we highlighted in Sect. 4.1, based on the new low- and high-luminosity AGN added in this study, it is now possible to recognize a more complex dependence of the hard X-ray bolometric correction on the λ_{EDD} in the data than the dependence that is represented by a simple linear relation. We then chose to fit the dependence of K_X on λ_{EDD} using the relation

$$K_X(\lambda_{EDD}) = a\left[1 + \left(\frac{\lambda_{EDD}}{b}\right)^c\right]. \quad (6)$$

Our best-fit relation (the parameters are provided in Table 3) is showed as a black solid line. Its average intrinsic spread, ~0.31 dex (black dotted lines), is larger than the spread found previously for the fitting relation using the bolometric luminosity as the independent variable (~0.27; see Sect. 4.1).

The same analysis was performed for the K_X–M_{BH} relation (right panel). Again, we find that a linear relation does not represent the whole dataset (see, e.g., the relation found by M17) because it would underestimate k_X at low λ_{EDD} and low M_{BH}. We therefore used the following equation to fit the data:

$$K_X(M_{BH}) = a\left[1 + \left(\frac{\log(M_{BH}/M_\odot)}{b}\right)^c\right]. \quad (7)$$

The best-fit relation (see Table 3) is shown as a black solid line. Its average intrinsic spread, ~0.35 dex (black dotted lines), is larger than the one previously found for the $K_X(\lambda_{EDD})$ and the $K_X(L_{BOL})$ relations (0.31 dex and 0.27 dex respectively).

In the lower panels of Fig. 9 we show the optical bolometric correction as a function of the λ_{EDD} (left panel) and the

Table 3. Best-fit parameters (see Eq. (2)) for the hard X-ray bolometric correction relation as a function of the Eddington ratio and the BH mass.

	a	b	c	Spread [dex]
λ_{EDD}	7.51 ± 1.34	0.05 ± 0.03	0.61 ± 0.07	0.31
M_{BH}	16.75 ± 0.71	9.22 ± 0.08	26.14 ± 3.73	0.35

Table 4. Best-fit parameters (see Eq. (5)) for the optical bolometric correction relation as a function of the Eddington ratio and the BH mass.

	k	Spread [dex]
λ_{EDD}	5.10 ± 0.13	0.22
M_{BH}	5.05 ± 0.35	0.21

M_{BH} (right panel). Black hexagons are the average values computed in bins of Eddington ratios and BH masses. As we found for $K_O(L_{BOL})$ the optical bolometric correction shows a roughly constant average value, $k \sim 5$, with a spread of ~0.22 dex (see Table 4).

7. AGN unobscured bolometric luminosity function

To verify the consistency of the bolometric corrections we computed above, we derived the type 1 AGN bolometric Luminosity Function (LF) to determine whether compatible results can be obtained starting from either optically selected or X-ray selected AGN LFs.

As shown by Ricci et al. (2017d), the type 1 optical LF agrees with the X-ray LF when only the unabsorbed ($N_H < 10^{21}-10^{22}$ cm^{-2}) sources are considered and the α_{OX} relation as computed by Lusso & Risaliti (2016) is adopted, convolved with an observational scatter of ~0.4 dex.

Based on this result, if the bolometric corrections derived in this work were consistent, the bolometric LFs computed either with K_O or K_X should produce similar LF in the bolometric domain. We show in Fig. 10 the resulting bolometric LFs in two representative redshift bins: $z \sim 1.25$ and ~2.8. The optical LF was parameterized with the double-powerlaw as derived by Palanque-Delabrouille et al. (2013) for redshift 1.25 and as derived by Ross et al. (2013) at $z \sim 2.80$. When needed, we converted the g-band optical LF into i-band $z = 2$ absolute magnitude adopting Eq. (8) of Ross et al. (2013), then we converted them into 2500 Å fluxes using the standard method outlined in Richards et al. (2006), and finally converted into 4500 Å fluxes assuming a power-law SED $L_\nu \propto \nu^{-\alpha}$ with $\alpha = 0.5$ (Vanden Berk et al. 2001, check footnote 5). Then we applied the best-fit optical bolometric corrections derived in Sect. 4.2 and convolved with its spread. The resulting curves are shown in Fig. 10 as red solid lines.

For the X-ray selected LF, we adopted the Ueda et al. (2014) 2–10 keV LF, which was computed in various absorption ranges (i.e., at different N_H). This means that in order to match the optically selected LF, only the AGN with $N_H < 10^{21}$ cm^{-1} were selected (Ricci et al. 2017d). We then converted the X-ray luminosity function into the bolometric LF using the $K_X(L_{BOL})$ (blue line in Fig. 10) bolometric correction derived in Sect. 4.1, taking its intrinsic spread into account.

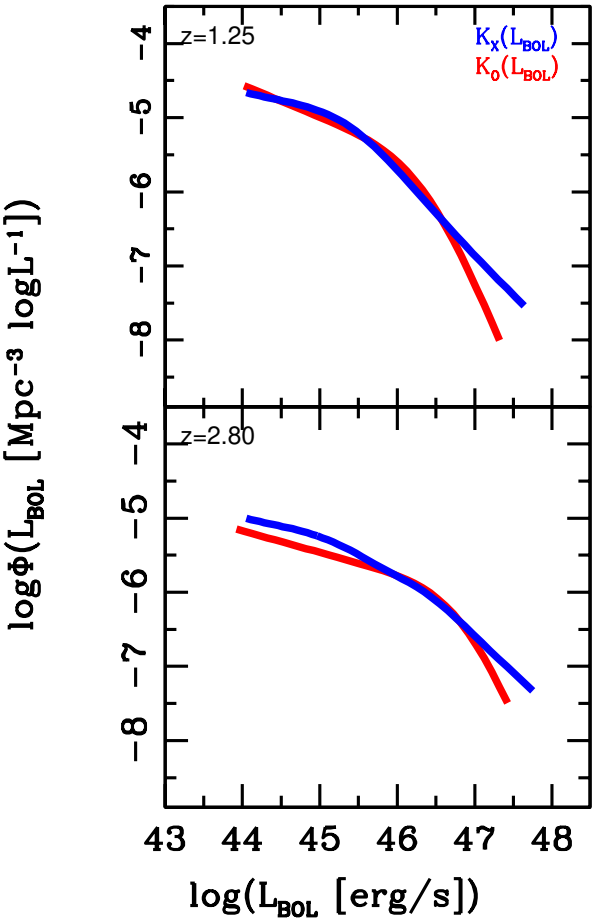

Fig. 10. AGN type 1 bolometric luminosity function computed in the two redshift bins ($z = 1.25$ and $z = 2.80$) adopting the X-ray and optical bolometric corrections as a function of the bolometric luminosity.

The two LFs agree fairly well within 0.2 dex in space density in the range $44 < \log(L_{BOL}/[\text{erg s}^{-1}]) < 47.5$.

A more accurate statistical analysis and precise computation of the AGN bolometric LF that takes the spread of the luminosity distributions and selection effects into account is beyond the scope of this paper (see, e.g., recent results on this topic by Shen et al. 2020). However, our findings lend further support to the validity of our bolometric corrections.

8. Discussion

The main result of our analysis is that type 1 and type 2 sources share the same bolometric correction in their ~4 dex wide overlapping luminosity regime. This allowed us to build a universal bolometric correction valid for about 7 dex in luminosity, where the low-luminosity regime is only probed by type 2 AGN and the high-luminosity regime by type 1 AGN. The similarity between the bolometric correction relations found for type 1 and type 2 AGN seems to favor the classical AGN unification scenario (Antonucci 1993, 2012; Urry & Padovani 1995), or at least any model in which the central emission mechanism is the same for both AGN populations.

Another interesting result is that the computed bolometric corrections (and then the central emission mechanisms) do not show any significant dependence on redshift up to $z \sim 3.5$, as expected if the bolometric corrections are determined by the physics of accretion and emission. Therefore, they can be safely

be used to study the accretion rate histories of the AGN in the past 11 Gyr.

The optical and hard X-ray bolometric corrections separately follow the same analytical behavior regardless the independent variable While the former remains always nearly constant, the latter shows a significant increase for the most luminous and massive AGN.

The ratio between the bolometric luminosity and the X-ray luminosity in AGN can be seen as the ratio between the total energy output dominated by the big blue bump component that is due to thermal UV emission from the accretion disk and the emission released by the X-ray corona. Accordingly, the correlation we observe between K_X and L_{BOL} supports a scenario in which the more the accretion disk emits, the less the corona radiative power contributes to the total energy output. This may suggest a change in the properties of the X-ray corona in the most powerful AGN that might be related to a stronger photon-trapping and advection of X-ray radiation in case of high accretion rates or the presence of UV radiation-driven accretion-disk winds affecting the corona (see M17, Nardini et al. 2019 and Zappacosta et al. 2020). This behavior seems to be typical of sources with extreme values of the total bolometric luminosity. Our findings agree with the existence of a correlation between the α_{OX} and the optical luminosity (estimated at 2500 Å), as shown by Lusso & Risaliti (2016), for example. We therefore computed the expected K_X if the relation between the X-ray luminosity and the optical luminosity by Lusso & Risaliti (2016) (in which $L_X \propto L_{UV}^{0.6}$) and a constant $K_O \sim 5$ (see the next Section for further details) are assumed[5]. As shown in Fig. 6 as a brown line, the resulting analytical prediction, that is, $K_X \propto L_{BOL}^{0.358}$, agrees fairly well with our best-fit relation, sharing a similar slope and normalization within the uncertainties. This comparison tells us that the bolometric correction relation and the α_{OX} slope are tightly related: the observed correlations are mainly due to the change in the X-ray emission fraction in the bolometric luminosity budget. In this framework, the X-ray bolometric correction is a better measure of this phenomenon, because it takes the whole energetic emission into account and does not suffer from the obscuration that might affect the UV/optical luminosity (especially in type 2 sources).

9. Summary and conclusions

We combined five AGN samples to characterize a general bolometric correction that is valid for the entire AGN population. We considered a total of 1009 AGN sources (501 of which are type 1 sources, and the remaining are 566 type 2) properly selected to cover the widest luminosity range ever sampled (with $41 < \log(L_{BOL}/[\mathrm{erg\,s^{-1}}]) < 48$), and within a redshift range from $z \sim 0$ up to $z \sim 4$. For 745 of these sources we have an estimate of the M_{BH}. We carried out a dedicated SED-fitting procedure. Our main results are listed below:

- We confirm that the hard X-ray bolometric correction, K_X, correlates with the bolometric luminosity L_{BOL} for the type 1 and the type 2 AGN populations. It is fairly constant at $\log(L_{BOL}/L_\odot) < 11$, but it increases to an order of magnitude at $\log(L_{BOL}/L_\odot) \sim 14.5$. The relations found for the type 1 and the type 2 samples are very similar and present the same average intrinsic spread (∼0.27 dex). Therefore, it has been possible to derive a universal hard X-ray bolometric correction that valid for type 1 and type 2 AGN.
- The K_X correction as a function of the hard X-ray luminosity gives on average the same X bolometric correction as when the L_{BOL} is the independent variable, with differences within 0.2 dex in the range $8 < \log(L_{BOL}/L_\odot) < 13$.
- We discussed how the positive trend we observe between the X-ray bolometric correction and the bolometric luminosity may be fit in the X-ray weakness scenario, according to which the X-ray emitting corona tends to be less powerful than the UV/optical emission, with increasing bolometric luminosity.
- The dependence of the optical (B-band, at 4400 Å) bolometric correction either on the bolometric luminosity or the optical luminosity shows an almost constant (i.e., $K_O \sim 5$) behavior, with an average intrinsic spread of ∼0.27 dex.
- We find that $K_X(L_{BOL})$ increases with increasing λ_{EDD} and M_{BH}, while $K_O(L_{BOL})$ is roughly constant with an average value of ∼5. This analysis suggests that the optical and the hard X-ray bolometric corrections separately follow the same analytical behavior, independently of which variable they are compared with.
- We find no dependence of the X-ray and optical bolometric corrections on redshift up to $z \sim 3.5$.
- We derived the type 1 AGN bolometric LF by converting the hard X-ray (optical) luminosity function using the hard X-ray (optical) bolometric correction as a function of the bolometric luminosity. We find that the X-ray and optical luminosity functions agree within 0.2 dex in the range $44 < \log(L_{BOL}/[\mathrm{erg\,s^{-1}}]) < 47.5$. We repeated the same analysis using the bolometric corrections as a function of the hard X-ray and optical luminosities, and in this case also retrieved a similarly good match.

We thus provide a universal bolometric correction, statistically representative of the entire X-ray selected AGN population, which spans about seven decades in luminosity and can be applied up to $z \sim 3.5$ in order to estimate the energetic budget of the AGN and their accretion rate history.

Acknowledgements. F. Ricci acknowledges financial support from FONDECYT Postdoctorado 3180506 and CONICYT project Basal AFB-170002. E. Piconcelli, A. Bongiorno, S. Bianchi acknowledge financial support from ASI and INAF under the contract 2017-14-H.0 ASI-INAF. C. Vignali acknowledges financial support from ASI-INAF I/037/12/0 and ASI-INAF n.2017-14-H.0. F. Shankar acknowledges partial support from a Leverhulme Trust Research Fellowship.

References

Aird, J., Coil, A. L., & Georgakakis, A. 2019, MNRAS, 484, 4360
Akiyama, M., Ueda, Y., Ohta, K., Takahashi, T., & Yamada, T. 2003, ApJS, 148, 275
Antonucci, R. 1993, ARA&A, 31, 473
Antonucci, R. 2012, Astron. Astrophys. Trans., 27, 557
Aversa, R., Lapi, A., de Zotti, G., Shankar, F., & Danese, L. 2015, ApJ, 810, 74
Baumgartner, W. H., Tueller, J., Markwardt, C. B., et al. 2013, ApJS, 207, 19
Berta, S., Lutz, D., Genzel, R., Förster-Schreiber, N. M., & Tacconi, L. J. 2016, A&A, 587, A73
Bischetti, M., Piconcelli, E., Vietri, G., et al. 2017, A&A, 598, A122
Bongiorno, A., Merloni, A., Brusa, M., et al. 2012, MNRAS, 427, 3103
Bongiorno, A., Schulze, A., Merloni, A., et al. 2016, A&A, 588, A78
Bruzual, G., & Charlot, S. 2003, MNRAS, 344, 1000
Calistro Rivera, G., Lusso, E., Hennawi, J. F., & Hogg, D. W. 2016, ApJ, 833, 98
Calzetti, D., Armus, L., Bohlin, R. C., et al. 2000, ApJ, 533, 682
Chabrier, G. 2003, PASP, 115, 763
Czerny, B., & Elvis, M. 1987, ApJ, 321, 305
de Vaucouleurs, G., de Vaucouleurs, A., Corwin, Jr., H. G., et al. 1991, Third Reference Catalogue of Bright Galaxies. Volume I: Explanations and References. Volume II: Data for Galaxies Between 0^h and 12^h. Volume III: Data for Galaxies Between 12^h and 24^h

[5] L_O was converted into $L_{UV} = L_{2500\,Å}$ by assuming a spectral slope of $\lambda^{-1.54}$ (Vanden Berk et al. 2001).

Duras, F., Bongiorno, A., Piconcelli, E., et al. 2017, A&A, 604, A67
Elvis, M., Wilkes, B., McDowell, J., et al. 1994, ApJS, 95, 1
Feltre, A., Hatziminaoglou, E., Fritz, J., & Franceschini, A. 2012, MNRAS, 426, 120
GildePaz, A., Boissier, S., Madore, B. F., et al. 2007, ApJS, 173, 185
Häring, N., & Rix, H.-W. 2004, ApJ, 604, L89
Ho, L. C., & Kim, M. 2014, ApJ, 789, 17
Hopkins, P. F., Richards, G. T., & Hernquist, L. 2007, ApJ, 654, 731
Kelly, B. C., Bechtold, J., Trump, J. R., Vestergaard, M., & Siemiginowska, A. 2008, ApJS, 176, 355
Koulouridis, E., Faccioli, L., Le Brun, A. M. C., et al. 2018, A&A, 620, A4
Krawczyk, C. M., Richards, G. T., Mehta, S. S., et al. 2013, ApJS, 206, 4
La Franca, F., Fiore, F., Comastri, A., et al. 2005, ApJ, 635, 864
La Franca, F., Melini, G., & Fiore, F. 2010, ApJ, 718, 368
Liu, Z., Merloni, A., Georgakakis, A., et al. 2016, MNRAS, 459, 1602
Lusso, E., & Risaliti, G. 2016, ApJ, 819, 154
Lusso, E., & Risaliti, G. 2017, A&A, 602, A79
Lusso, E., Comastri, A., Vignali, C., et al. 2010, A&A, 512, A34
Lusso, E., Comastri, A., Simmons, B. D., et al. 2012, MNRAS, 425, 623
Magorrian, J., Tremaine, S., Richstone, D., et al. 1998, AJ, 115, 2285
Marchese, E., Della Ceca, R., Caccianiga, A., et al. 2012, A&A, 539, A48
Marconi, A., & Hunt, L. K. 2003, ApJ, 589, L21
Marconi, A., Risaliti, G., Gilli, R., et al. 2004, in The Interplay Among Black Holes, Stars and ISM in Galactic Nuclei, eds. T. Storchi-Bergmann, L. C. Ho, & H. R. Schmitt, IAU Symp., 222, 49
Martocchia, S., Piconcelli, E., Zappacosta, L., et al. 2017, A&A, 608, A51
Miller, L., Peacock, J. A., & Mead, A. R. G. 1990, MNRAS, 244, 207
Nardini, E., Lusso, E., Risaliti, G., et al. 2019, A&A, 632, A109
Netzer, H. 2019, MNRAS, 488, 5185
Onori, F., La Franca, F., Ricci, F., et al. 2017a, MNRAS, 464, 1783
Onori, F., Ricci, F., La Franca, F., et al. 2017b, MNRAS, 468, L97
Palanque-Delabrouille, N., Magneville, C., Yèche, C., et al. 2013, A&A, 551, A29
Pierre, M., Pacaud, F., Adami, C., et al. 2016, A&A, 592, A1
Pozzi, F., Vignali, C., Comastri, A., et al. 2007, A&A, 468, 603
Ricci, C., Trakhtenbrot, B., Koss, M. J., et al. 2017a, ApJS, 233, 17
Ricci, F., La Franca, F., Marconi, A., et al. 2017b, MNRAS, 471, L41
Ricci, F., La Franca, F., Onori, F., & Bianchi, S. 2017c, A&A, 598, A51
Ricci, F., Marchesi, S., Shankar, F., La Franca, F., & Civano, F. 2017d, MNRAS, 465, 1915
Richards, G., Lacy, M., Storrie-Lombardi, L., et al. 2006, ApJS, 166, 470
Ross, N. P., McGreer, I. D., White, M., et al. 2013, ApJ, 773, 14
Runnoe, J. C., Brotherton, M. S., & Shang, Z. 2012a, MNRAS, 422, 478
Runnoe, J. C., Brotherton, M. S., & Shang, Z. 2012b, MNRAS, 426, 2677
Salucci, P., & Persic, M. 1999, MNRAS, 309, 923
Sanders, D. B., Phinney, E. S., Neugebauer, G., Soifer, B. T., & Matthews, K. 1989, ApJ, 347, 29
Sanders, D. B., Mazzarella, J. M., Kim, D.-C., Surace, J. A., & Soifer, B. T. 2003, AJ, 126, 1607
Shankar, F., Salucci, P., Granato, G. L., De Zotti, G., & Danese, L. 2004, MNRAS, 354, 1020
Shankar, F., Bernardi, M., Sheth, R. K., et al. 2016, MNRAS, 460, 3119
Shankar, F., Bernardi, M., Richardson, K., et al. 2019, MNRAS, 485, 1278
Shen, X., Hopkins, P. F., Faucher-Giguère, C. A., et al. 2020, MNRAS, submitted [arXiv:2001.02696]
Shimizu, T. T., Meléndez, M., Mushotzky, R. F., et al. 2016, MNRAS, 456, 3335
Silva, L., Maiolino, R., & Granato, G. L. 2004, MNRAS, 355, 973
Soltan, A. 1982, MNRAS, 200, 115
Spinoglio, L., Andreani, P., & Malkan, M. A. 2002, ApJ, 572, 105
Stalevski, M., Ricci, C., Ueda, Y., et al. 2016, MNRAS, 458, 2288
Steffen, A. T., Strateva, I., Brandt, W. N., et al. 2006, AJ, 131, 2826
Tananbaum, H., Avni, Y., Branduardi, G., et al. 1979, ApJ, 234, L9
Tremaine, S., Gebhardt, K., Bender, R., et al. 2002, ApJ, 574, 740
Ueda, Y., Akiyama, M., Ohta, K., & Miyaji, T. 2003, ApJ, 598, 886
Ueda, Y., Akiyama, M., Hasinger, G., Miyaji, T., & Watson, M. G. 2014, ApJ, 786, 104
Urry, C. M., & Padovani, P. 1995, PASP, 107, 803
Vanden Berk, D. E., Richards, G. T., Bauer, A., et al. 2001, AJ, 122, 549
Vasudevan, R. V., & Fabian, A. C. 2007, MNRAS, 381, 1235
Vasudevan, R. V., Mushotzky, R. F., Winter, L. M., & Fabian, A. C. 2009, MNRAS, 399, 1553
Vasudevan, R. V., Fabian, A. C., Gandhi, P., Winter, L. M., & Mushotzky, R. F. 2010, MNRAS, 402, 1081
Vietri, G., Piconcelli, E., Bischetti, M., et al. 2018, A&A, 617, A81
Vignali, C., Brandt, W. N., & Schneider, D. P. 2003, AJ, 125, 433
Vittorini, V., Shankar, F., & Cavaliere, A. 2005, MNRAS, 363, 1376
Volonteri, M., Haardt, F., & Madau, P. 2003, ApJ, 582, 559
Wiebe, D. V., Ade, P. A. R., Bock, J. J., et al. 2009, ApJ, 707, 1809
Zappacosta, L., Piconcelli, E., Giustini, M., et al. 2020, A&A, 635, L5

Appendix A: Physical properties of the samples

Table A.1. Properties of the *Swift* type 2 and type 1 sources.

Name (1)	z (2)	$\log L_{\rm X}$ (3)	$\log L_{\rm BOL}$ (4)	$\log L_{\rm O}$ (5)	$\log M_{\rm BH}$ (6)
		Type 2 sources			
IRAS F 05189−2524	0.0426	43.40	45.26	–	7.45
2MASX J07595347+2323241	0.0292	43.25	43.95	–	7.78
MCG -01-24-12	0.0196	43.24	44.18	–	7.16
NGC 1275	0.0176	43.98	44.74	–	7.46
Mrk 348	0.0150	43.44	44.24	–	7.23
Mrk 1210	0.0135	43.13	44.07	–	6.78
ESO 234-G -050	0.0088	41.60	42.97	–	6.00
NGC 2992	0.0077	42.00	42.74	–	6.72
NGC 7465	0.0065	41.97	43.40	–	6.54
NGC 5506	0.0062	42.99	44.15	–	6.86
NGC 1365	0.0055	42.32	43.71	–	6.65
NGC 1052	0.005	41.62	42.55	–	6.63
NGC 6221	0.0050	41.20	42.64	–	6.46
NGC 7314	0.0048	42.33	43.26	–	6.24
NGC 4395	0.0013	40.50	41.43	–	5.14
PKS 0326−288	0.108	44.52	45.42	–	–
NGC 3079	0.0372	41.30	42.75	–	–
Mrk 417	0.0327	43.73	44.65	–	–
NGC 612	0.0298	43.94	44.76	–	–
NGC 788	0.0136	43.02	43.76	–	–
NGC 3281	0.0107	43.12	44.23	–	–
NGC 4388	0.0084	43.05	43.98	–	–
ESO 005−G004	0.0062	42.78	43.95	–	–
NGC 5643	0.004	42.43	43.60	–	–
NGC 4941	0.0037	41.25	42.18	–	–
NGC 4138	0.003	41.23	42.49	–	–
		Type 1 sources			
Mrk 876	0.129	44.19	45.34	–	8.54
Mrk 1383	0.087	44.19	45.42	44.89	9.31
Mrk 771	0.063	43.60	45.01	–	7.94
Mrk 509	0.034	44.08	44.99	44.48	8.08
Mrk 817	0.031	43.49	44.60	44.08	7.90
Mrk 279	0.030	43.41	44.68	44.28	7.59
Mrk 335	0.026	43.24	44.51	44.29	7.21
Mrk 590	0.026	42.70	43.76	–	7.60
Mrk 79	0.022	43.11	44.18	43.92	8.02
NGC 5548	0.017	43.14	44.21	43.95	7.87
NGC 7469	0.016	43.19	44.42	44.14	7.42
NGC 4748	0.015	42.34	43.72	–	6.58
NGC 4253	0.013	42.71	43.77	–	6.21
NGC 3783	0.010	43.43	44.24	43.37	7.38
NGC 3516	0.009	42.72	43.85	–	7.59
NGC 4593	0.009	42.81	43.72	–	7.06
NGC 6814	0.005	42.31	43.64	–	7.30
NGC 3227	0.004	42.10	43.23	–	7.45
NGC 4151	0.003	42.31	43.66	43.28	7.66
NGC 4051	0.002	41.33	43.03	–	6.43

Notes. (1) Source name; (2) redshift (Baumgartner et al. 2013); (3) intrinsic logarithmic hard X-ray luminosity (2–10 keV) in erg s^{-1} units from Ricci et al. (2017a); (4) SED-fitting derived logarithmic bolometric luminosity in erg s^{-1} units; (5) B-band 4400 Å AGN logarithmic luminosity in erg s^{-1} units from the photometric data, provided only for type I sources, because the contamination from the galaxy is negligible; (6) logarithmic $M_{\rm BH}$ in $M_{\odot}$ from Onori et al. (2017b) for the type 2 sources and from Ricci et al. (2017c) for the type 1 sources.

Table A.2. Properties of the X-WISSH sample.

Name (1)	z (2)	$\log L_{\rm X}$ (3)	$\log L_{\rm BOL}$ (4)	$\log L_{\rm O}$ (5)	$\log M_{\rm BH}$ (6)
J0045+1438	1.992	44.24	47.38	46.76	–
J0209−0005	2.856	45.16	47.62	46.99	–
J0735+2659	1.982	45.11	47.65	47.03	–
J0745+4734	3.225*	46.37	48.01	47.40	10.20
J0747+2739	4.11	45.43	47.44	46.88	–
J0801+5210	3.263*	45.25	47.84	47.13	9.79
J0900+4215	3.294*	46.00	47.93	47.38	9.32
J0904+1309	2.974	45.89	47.78	47.17	–
J0947+1421	3.040	45.01	47.67	47.02	–
J1014+4300	3.126	45.43	47.85	47.24	–
J1027+3543	3.112	45.79	48.00	47.32	–
J1057+4555	4.140	45.77	47.91	47.36	–
J1106+6400	2.220*	45.69	47.78	47.10	10.00
J1110+4831	2.957	45.36	47.81	47.21	–
J1111+1336	3.492*	45.36	47.69	47.06	9.93
J1159+1337	3.984	45.04	47.74	47.18	–
J1200+3126	2.993	45.55	47.84	47.18	–
J1201+1206	3.512*	45.77	47.77	47.21	9.51
J1215−0034	2.707	45.33	47.62	46.96	–
J1236+6554	3.424*	45.33	47.65	46.98	9.63
J1245+0105	2.798	45.03	47.25	–	–
J1249−0159	3.638	45.08	47.55	46.97	–
J1250+2631	2.044	45.94	47.91	47.32	–
J1328+5818	3.133	45.22	47.20	–	–
J1333+1649	2.089	45.83	47.73	47.07	–
J1421+4633	3.454*	45.18	47.65	47.09	9.79
J1426+6025	3.189	45.72	48.07	47.42	–
J1441+0454	2.059	44.84	47.34	46.47	–
J1513+0855	2.897	45.60	47.67	47.12	–
J1521+5202	2.218	44.85	47.91	47.28	9.99
J1549+1245	2.365*	45.34	47.81	47.03	10.10
J1621−0042	3.710	46.04	47.81	47.22	–
J1639+2824	3.801	45.67	48.05	47.38	–
J1701+6412	2.727	45.75	48.01	47.36	–
J2123−0050	2.281*	45.43	47.72	47.09	9.59

Notes. (1) Source name; (2) redshift from SDSS or from Vietri et al. (2018) (marked with an asterisk); (3) intrinsic logarithmic hard X-ray luminosity (2–10 keV) in erg s^{-1} units, from Martocchia et al. (2017); (4) SED-fitting derived logarithmic bolometric luminosity in erg s^{-1} units; (5) B-band 4400 Å AGN logarithmic luminosity in erg s^{-1} units, from the photometric data when present; (6) logarithmic BH mass in $M_{\odot}$ units, from Vietri et al. (2018).

Table A.3. Properties of the ASCA sample.

Name (1)	z (2)	$\log L_{\rm X}$ (3)	$\log L_{\rm BOL}$ (4)	$\log L_{\rm O}$ (5)
		Type 2 sources		
J235554+2836	0.729	44.87	46.36	–
J130453+3548	0.316	43.91	44.79	–
J090053+3856	0.229	43.94	44.54	–
J234725+0053	0.213	43.93	45.19	–
J111432+4055	0.153	43.77	44.25	–
J150339+1016	0.095	43.26	43.80	–
		Type 1 sources		
J001913+1556	2.270	45.71	46.76	46.54
J015840+0347	0.658	44.75	46.35	45.36
J125732+3543	0.524	44.56	45.69	45.21
J002619+1050	0.474	44.24	45.50	45.02
J023520−0347	0.376	44.23	45.65	44.89
J151441+3650	0.371	44.83	45.96	45.30
J144055+5204	0.320	44.19	45.43	44.89
J000927−0438	0.314	43.95	44.78	44.34
J121427+2936	0.309	44.25	45.03	44.90
J122017+0641	0.287	44.33	45.27	44.79
J142353+2247	0.282	44.25	45.12	44.44
J172938+5230	0.278	44.13	45.41	44.98
J103934+5330	0.229	43.62	44.61	44.12
J233253+1513	0.215	44.13	44.98	44.54
J121854+2957	0.178	43.64	45.16	43.63
J170305+4526	0.171	43.68	44.97	44.50
J140528+2224	0.156	43.44	44.52	44.11
J121359+1404	0.154	43.26	44.36	43.92
J170548+2412	0.114	43.26	44.60	43.90
J134450+0005	0.087	42.95	44.25	43.91
J121930+0643	0.081	43.00	44.52	44.14
J144109+3520	0.077	42.64	43.95	43.66

Notes. Source name; (2) redshift; (3) intrinsic logarithmic hard X-ray luminosity (2–10 keV) in erg s^{-1} units from Liu et al. (2016) rescaled for our adopted cosmology; (4) SED-fitting derived logarithmic bolometric luminosity in erg s^{-1} units; (5) B-band 4400 Å AGN logarithmic luminosity in erg s^{-1} units from the photometric data, provided only for type I sources, because the contamination from the galaxy is negligible.

Table A.4. Properties of the XXL sample.

Name (1)	z (2)	$\log L_X$ (3)	$\log L_{BOL}$ (4)	$\log L_O$ (5)	$\log M_{BH}$ (6)
1237679323935212347	5.0111	45.24	47.10	46.38	9.42
1237679253060517914	3.1977	44.86	46.71	45.82	8.60
1237679253062091149	3.1737	45.12	46.54	45.75	8.24
1237679322324271694	3.0009	44.84	46.58	45.51	8.19
1237679323399389313	2.7648	45.57	46.70	46.08	9.41
1237679439888187748	2.7638	44.82	46.24	–	8.10
1237679324471623799	2.71	45.16	46.94	46.27	9.11
1237679253060780145	2.7074	44.81	46.64	45.97	9.43
1237679323398013411	2.647	45.02	46.44	45.95	8.76
1237679254134259865	2.6351	44.93	47.07	46.44	9.81
1237679323399061589	2.6016	44.97	47.06	46.40	9.70
1237679322324992234	2.3271	45.02	46.31	45.59	8.76
1237679322861601161	2.2212	44.76	46.07	45.23	7.95
1237679322324336823	2.0902	44.70	46.50	45.94	8.77
1237679321787662348	2.0375	45.09	47.08	–	9.93
1237679254135505041	2.0092	45.14	46.41	45.85	9.09
1237678887988167005	1.9572	44.58	46.27	45.36	7.91
1237679254672113748	1.9153	44.74	46.25	45.64	8.85
1237679323934621916	1.8757	44.96	46.89	46.01	9.24
1237679322862256290	1.871	45.29	47.22	46.67	9.91
1237679253060714853	1.8508	44.37	46.17	45.38	8.36
1237679322862321678	1.7039	44.97	46.97	46.41	9.59
1237679255209115743	1.6757	44.90	46.53	45.92	8.95
1237669770301735049	1.6423	44.56	46.28	45.65	8.39
1237679253598044260	1.5449	44.58	46.59	45.90	9.34
1237679253597782176	1.397	44.59	46.73	46.04	9.33
1237669770301669421	1.371	44.81	46.62	46.01	9.39
1237679255745986570	1.2249	44.53	46.69	46.02	9.19
1237679323399127053	1.1815	44.25	46.68	46.12	9.27
1237679253599092740	1.1644	44.65	46.63	45.84	8.87
1237679322322632786	0.8909	44.29	46.09	45.53	8.30

Notes. (1) Source name; (2) redshift; (3) intrinsic logarithmic hard X-ray luminosity (2–10 keV) in erg s^{-1} units; (4) SED-fitting derived logarithmic bolometric luminosity in erg s^{-1} units; (5) B-band 4400 Å logarithmic luminosity in erg s^{-1} units from the photometric data when present; (6) logarithmic M_{BH} in $M_\odot$ unit.